Journal of
Materials Chemistry B

ROYAL SOCIETY
OF CHEMISTRY

PAPER

View Article Online
View Journal | View Issue

Check for updates

Cite this: *J. Mater. Chem. B*, 2024, **12**, 9056

Unleashing the antibacterial and antibiofilm potential of silica-based nanomaterials functionalized with an organotin(IV) compound†

Victoria García-Almodóvar,[ab] Perla del Rosario Ardiles,[b] Sanjiv Prashar,[a] Paulina Laura Páez *[b] and Santiago Gómez-Ruiz *[a]

Bacterial diseases caused by superbugs are expected to be the main cause of death worldwide within a decade as a consequence of the resistance they are acquiring to the antibiotics currently in use, therefore, the field of new antibacterial treatments is currently being thoroughly studied. The present work focuses on the synthesis, functionalization, characterization and antibacterial behaviour of different systems based on three different silica-based nanostructured materials (MSN, mesoporous silica nanoparticles, SBA-15 Santa Barbara amorphous-15 and FSP fibrous slica nanoparticles) which serve as scaffolds for the support of different platforms to target and treat bacterial diseases and biofilm formation. Thus, (3-carboxypropyl)triphenylphosphonium bromide (PPh_3^+) and a cytotoxic organotin(IV) fragment (Sn) have been incorporated in the silica-based materials to study their potential activity in different antibacterial applications. After a complete characterization of the synthesized systems, which confirmed the incorporation of both the targeting and the therapeutic fragments within the nanostructured materials, the antibacterial study of the materials demonstrated bactericidal capacity against *Escherichia coli* and perturbation of the bacteria metabolism *via* oxidative stress through an enhanced ROS (reactive oxygen species) production. In addition, biofilm inhibition and eradication tests of bacterial strains were carried out, showing that the activity of the materials in both biofilm inhibition and eradication is dependent on the concentration of the material. Furthemore, the material MSN-AP(1:1)-PPh_3^+-Sn containing the targeting triphenylphosphonium and a "$SnPh_3$" fragment is capable of inhibiting and eradicating up to 50% of the formation of biofilms, which is outstanding for metallodrug-functionalized silica-based systems compared with other materials based on metal nanoparticles supported on silica. Finally, a hemolysis study was carried out with the nanostructured systems proving to be non-toxic, making them adequate for their subsequent use in preclinical trials through *in vivo* models.

Received 21st May 2024,
Accepted 7th August 2024

DOI: 10.1039/d4tb01106f

rsc.li/materials-b

1. Introduction

The treatment of bacterial diseases has undergone significant transformation since the discovery of penicillin by Alexander Fleming in 1928, with a wide array of antibiotic drugs such as ciprofloxacin and amoxicillin becoming mainstays of medical practice.[1] However, the growing issue of antibiotic resistance presents a global public health challenge. This phenomenon intersects with a variety of fields, including food security, climate change, and health infrastructure stability, necessitating a multidisciplinary approach known as the "One Health" perspective.[2–4] The spread of resistant bacteria across human, animal, and environmental sectors, as well as the circulation of resistance determinants between these sectors worldwide, poses a major threat to global health. The persistence and spread of resistant microbial species at the human–animal–environment interface can alter microbial genomes, leading to the emergence of resistant superbugs across various ecological niches.[5,6]

Given the significant threat posed by antibiotic-resistant bacteria, there has been an upsurge in research focusing on novel antibacterial treatments.[7] Recently, metals such as silver, copper, and tin have emerged as promising candidates for antibacterial treatments, both as nanoparticles and metal complexes.

---

[a] *COMET-NANO Group, Departamento de Biología y Geología, Física y Química Inorgánica, ESCET, Universidad Rey Juan Carlos, Calle Tulipán s/n, E-28933 Móstoles, Madrid, Spain. E-mail: santiago.gomez@urjc.es*

[b] *Departamento de Ciencias Farmacéuticas, Facultad de Ciencias Químicas, Universidad Nacional de Córdoba, Ciudad Universitaria, Haya de la Torre y Medina Allende, X5000HUA Córdoba, Argentina. E-mail: plpaez@unc.edu.ar*

† Electronic supplementary information (ESI) available. See DOI: https://doi.org/10.1039/d4tb01106f

In this study, we introduce the use of silica-based nanostructured materials as carrier platforms for different agents, aiming to explore their potential as novel antibacterial systems. Silica-based porous materials offer numerous advantages, including a high surface area (>1000 m^2 g^{-1}), customizable internal and external surfaces, biocompatibility, varied pore sizes, and a range of functionalization methods for tailored nanosystem design.[8] These properties enable the creation of versatile mesoporous silica nanoparticles with varying morphology, pore size, pore distribution, and other textural, physical, and chemical characteristics, especially in a biological context.[9]

On one hand, there has been an increase in research focused on the treatment of bacterial diseases and the eradication of superbugs. On the other, silicon-based nanomaterials are well-known for their use as drug encapsulating agents. In recent years, this area of research has grown significantly. Nanoparticles are being utilized to encapsulate antimicrobial peptides (AMPs) to enhance their stability and facilitate their application in the body.[10] They are also employed to deliver photosensitive compounds to specific treatment areas.[11] Some studies have developed hybrid nanomaterials that combine silica-based nanomaterials with polymers such as PVP[12] or even with silver nanoparticles, the latter being extensively studied for their antibacterial properties.[13] Additionally, silica nanoparticles are used to encapsulate certain FDA-approved drugs, which can lose efficacy over time due to pathogen resistance.[14]

The silica systems utilized in this work include: (a) mesoporous silica nanoparticles (MSN),[15] known for their spherical morphology and hexagonal pore arrangement; (b) Santa Barbara amorphous-15 (SBA-15),[16] characterized by their oval morphology and hexagonal pore distribution; and (c) fibrous silica particles (FSP),[17] featuring a fibrous, dandelion-shaped morphology with channels within the fibers for internal and external surface functionalization.

These silica nanoparticles can be functionalized with various compounds, and their biological action can occur through classical or non-classical mechanisms. Classical strategies involve surface adsorption with stimuli-responsive release (*e.g.*, pH change, electrochemical impulse, UV light),[18] whereas non-classical strategies involve robust covalent bonds for functionalization on both internal and external surfaces, providing biological activity without the need for therapeutic fragment release.[19]

In our study, the first compound of interest is (3-carboxypropyl) triphenylphosphonium bromide (PPh_3^+), a mitochondrial-targeting compound repurposed here to test its potential capability in competing against the double membrane of large negative bacteria due to the morphological similarities with mitochondrial membranes.[20]

In general, thiphenylphosphonium salts help in targeting bacteria,[21–24] therefore, we have combined triphenylphosphonium fragments with organotin(IV) agents (Sn) to leverage their potential advantages, including simplifying synthetic procedures and lowering doses for enhanced antibacterial and antibiofilm activity. This strategy aims to maximize the benefits of organotin(IV)[25] while minimizing potential drawbacks, as previous studies have shown that metallodrugs are largely effective against bacteria without inducing resistance.[26]

Our investigation assesses the antibacterial efficacy of the developed silica-based nanomaterials with triphenylphosphonium targeting and "$SnPh_3$" fragments against *Staphylococcus aureus* and *Escherichia coli* strains. The results reveal that these systems are capable of inhibiting and eradicating up to 50% of biofilm formation, outperforming other metal nanoparticles supported on silica and revealing as a plausible alternative to current biofilm-targeting approaches.[27] Furthermore, hemolysis studies confirm the non-toxic nature of the nanostructured systems, supporting their potential application in preclinical trials and *in vivo* models.

2. Materials and methods

2.1. Synthesis and functionalization of materials

2.1.1. General synthesis and characterization conditions. All the general conditions relating to reagents, synthetic protocols and characterization techniques can be found in the ESI.† This section contains only a short description of the specific synthesis and functionalization procedures.

2.1.2. Synthesis of mesoporous silica nanoparticles (MSN). MSN were prepared by using a sol–gel method described by Zhao *et al.*[15] A solution of CTAB surfactant (hexadecyltrimethylammonium bromide, 1.0 g, 2.74 mmol) was prepared in 480 mL of Milli-Q water. The solution was adjusted to a basic pH with the addition of NaOH (3.50 mL, 2 M) in a round-bottom flask. Once the mixture reached 80 °C under vigorous magnetic stirring, TEOS (tetraethyl orthosilicate, 5.00 mL, 22.40 mmol) was gradually added as the silica source. The reaction mixture was allowed to react for 2 hours. After the reaction, the resulting mixture was filtered to obtain a white solid. The solid was washed with Milli-Q water (2 × 250 mL) and methanol (1 × 250 mL). To remove any residual surfactant within the pores of the nanoparticles, the material was calcined at 550 °C for 24 hours, yielding the final product.

2.1.3. Synthesis of Santa Barbara amorphous-15 nanostructured material (SBA). The synthesis of SBA-15 followed a method similar to that used for MSN preparation, with slight modifications as described by Zhao and coworkers.[16] The reaction took place in a round-bottom flask, where Pluronic 123 (24 g, 4.14 mmol) was dissolved in a homogeneous mixture of water (180 mL) and hydrochloric acid (720 mL, 2 M). Under vigorous magnetic stirring, TEOS (54.66 mL, 24.5 mmol) was gradually added drop by drop. The mixture was allowed to react for 20 hours at 35 °C. After the initial reaction period, the mixture was left to stand for 24 hours at 80 °C. The final material was obtained using the same washing and calcining protocol as described for MSN synthesis, ensuring removal of any remaining surfactant, and yielding the desired SBA-15 material.

2.1.4. Synthesis of fibrous silica particles (FSP). The synthesis of fibrous silica particles (FSP) followed the protocol described by Sadeghzadeh and coworkers,[17] with some modifications. The hydrothermal method involved the preparation of a solution consisting of CPB (cetylpyridinium bromide hydrate, 1 g, 2.60 mmol) and urea (1.2 g, 19.98 mmol) dissolved in 60 mL of Milli-Q water, which was stirred vigorously for 15 minutes. To this solution, a homogeneous mixture of cyclohexane and 1-pentanol (60 : 3 mL) along with TEOS (5 mL, 22.39 mmol) was added drop by drop. The reaction mixture was stirred for 45 minutes before being transferred to a hydrothermal reactor, where it was left to react for 5 hours at 120 °C. The same washing and calcining protocol as for MSN and SBA-15 was applied to obtain the final FSP particles, ensuring removal of any residual surfactant or impurities.

2.1.5. Functionalization with 3-(aminopropyl)triethoxysilane (AP). To functionalize the previously synthesized silica nanomaterials, the systems must first be activated by placing them under vacuum at 90 °C for 24 hours, effectively removing any residual water molecules from the nanomaterials surface. Once activated, 20 mL of dried toluene and AP were added in a 1 : 0.1 ratio for the three materials (MSN, SBA, and FSP). For MSN, an additional fourth material was prepared with an AP ratio of 1 : 1. The mixtures were subjected to vigorous magnetic stirring at 110 °C for 48 hours. Following the reaction, the functionalized materials (MSN-AP(10), MSN-AP(1:1), SBA-AP(10), FSP-AP(10)) were collected by centrifugation and washed with toluene (2 × 20 mL) and diethyl ether (2 × 20 mL). The final materials were dried at 80 °C to yield the desired product.

2.1.6. Functionalization with (3-carboxypropyl)triphenylphosphonium bromide (PPh_3^+). An EDAC-type reaction was carried out by dissolving PPh_3^+ (40 mg), EDAC (*N*-(3-dimethylaminopropyl)-*N*′-ethylcarbodiimide hydrochloride, 32 mg), and NHS (*N*-hydroxysuccinimide, 48 mg) in a homogeneous mixture comprising DMSO (10 mL) and MES buffer ((*N*-morpholino)ethanesulfonic acid, 40 mL), allowing the reaction to proceed for 15 minutes at room temperature under vigorous magnetic stirring. Following this, each material (400 mg) was introduced into the reaction mixture and allowed to react for 2 hours more. To obtain the functionalized materials (MSN-AP(10)-PPh_3^+; MSN-AP(1:1)-PPh_3^+; SBA-AP(10)-PPh_3^+; FSP-AP(10)-PPh_3^+), the reaction mixture was centrifuged, and the resulting precipitate washed with DMSO (2 × 20 mL) and ethanol (2 × 20 mL), followed by drying at 80 °C.

2.1.7. Formation of the organotin(IV) complex (Sn) and incorporation into materials. The preparation of the material was carried out following similar procedures than those reported by our group.[28] To synthesize the organotin(IV) compound $Ph_3Sn\{SCH_2CH_2CH_2CH_2Si(OEt)_3\}$, triphenyltin(IV) chloride and 3-mercaptopropyltriethoxysilane were reacted with triethylamine in a 1 : 1 : 2 ratio under vigorous magnetic stirring for 24 hours at 80 °C under a nitrogen atmosphere. Following the organotin(IV) compound formation, the materials from the previous section underwent two vacuum/nitrogen cycles and were redispersed in toluene while maintaining an inert atmosphere. The supernatant resulting from the reaction of the organotin(IV) complex with each material, obtained at a material : Sn ratio of 1 : 0.1, was then filtered and allowed to react under vigorous magnetic stirring at 110 °C for 24 hours. Finally, to obtain the final materials (MSN-AP(10)-PPh_3^+-Sn; MSN-AP(1:1)-PPh_3^+-Sn; SBA-AP(10)-PPh_3^+-Sn; FSP-AP(10)-PPh_3^+-Sn), the materials were centrifuged and washed with toluene (2 × 20 mL) and ethanol (2 × 20 mL) before being dried at 80 °C.

2.2. Studies on the behaviour of materials in biological media

2.2.1. Sn release studies in physiologic medium. Before testing the activity of the final materials as potential agents for the inhibition of bacterial growth, it was necessary to estimate their behaviour in the simulated biological medium. Therefore, 1 mg mL^{-1} dispersions of the final materials were made in PBS at pH = 7.4 and incubated for 1, 4 and 24 hours at 37 °C and shaking conditions. After this time, the samples were centrifuged, and the supernatant was filtered to measure the amount of Sn released to the medium by the materials by ICP-MS at the time periods at which the rest of the antibacterial assays were also carried out (1, 4 and 24 hours).

2.2.2. Antibacterial activity of the synthesized materials. The studied strains were *Staphylococcus aureus* ATCC29213 (*S. aureus*) and *Escherichia coli* ATCC25922 (*E. coli*). Both strains were stored at −80 °C until they are used in the *in vitro* studies. They were then plated on Trypticase soy agar (TSA) medium prior to use in an assay, leaving them at 37 °C overnight. All assays were performed following the standardized protocols according to the Clinical and Laboratory Standards Institute (CLSI).[29]

2.2.3. Diffusion test. An inoculum of 0.5 in McFarland scale was sown in three directions in a Petri dish of Mueller Hinton agar (MHA) medium; then, 40 μL of each material at a concentration of 2 mg mL^{-1} in DMSO (both intermediate and final materials) were added in wells of 8 mm performed in the agar. This assay also considered a negative control well (PBS) and a positive control (ciprofloxacin, 5 μg). The results were determined considering the inhibition diameter of each material, taking into account the diameter of the well itself of 8 mm ± 1 mm.

2.2.4. Minimum inhibitory concentration (MIC). It was necessary to perform a McFarland inoculum again as in the previous section, but this time it needed to be diluted to a concentration of 10^6 CFU mL^{-1} (colony forming units in mL) in Mueller Hinton Broth medium (MHB). A dispersion of 2 mg of each final material was then carried out in 1 mL of DMSO and in a p96 plate several serial dilutions (1/2) were performed in MHB medium achieving a concentration range of 1000–0.5 μg mL^{-1}. The previously prepared inoculum was then added in a 1 : 1 ratio respect to the material and incubated for 24 h at 37 °C. After this time the MIC (minimum concentration at bacterial growth was not observed) can be noted by the simple turbidity of the well, but to confirm the MIC value, 3 μL of a solution of resazurin sodium salt (1 mg mL^{-1} in distilled H_2O) was added to each well, leaving it to react for 30 minutes at 37 °C. Thus, it couldbe observed that the wells in all blue colours show bacterial death and the wells in pink colours show bacterial viability.

2.2.5. Minimum bactericidal concentration (MBC). To check the minimum bactericidal concentration, a protocol based on microdrop culture was carried out. Before adding resazurin in the MIC assay, 20 μL of each MIC well and three concentrations above the MIC were taken and deposited as microdroplets in an MHA Petri dish and incubated for 24 h at 37 °C. After the incubation time, the CFU in each microdrop was counted and expressed as CFU mL^{-1}, thus allowing the percentage of bacterial death caused by each material to be calculated.

2.2.6. Death curves. In this assay an overnight inoculum was used, for this purpose a bacterial suspension in Trypticase soy broth (TSB) medium was incubated at 37 °C with materials at 2 mg mL^{-1} concentration in DMSO. 500 μL of inoculum and each material are incubated in a 1 : 1 ratio at 37 °C for 1, 4 and 24 h. Then, serial dilutions of the mixture were made in a 1 : 0.1 ratio. Finally, 20 μL of these dilutions were seeded in TSA Petri dishes and incubated for 24 h at 37 °C in order to count the CFU mL^{-1}.

2.2.7. Oxidative stress and reactive oxygen species (ROS). Inoculum at the same concentration to that prepared for the death curve assay as were the materials. In a dark p96 plate, the inoculum, and the dispersions of the materials (2 mg mL^{-1}) were added in triplicate in each well in a 1 : 1 ratio, at this point it was important to consider a control with inoculum and PBS. The plate was left to incubate for 1, 4 and 24 h at 37 °C. After the incubation times, 20 μL of the probe 2′,7′-dichlorofluorescein diacetate (DCF) 50 μM was added to each well and incubated for 30 minutes at 37 °C. The fluorescence intensity was measured in a spectrofluorometer Biotek Synergy HT with the excitation and emission wavelengths at 480 and 520 nm, respectively.

2.2.8. Nitrite formation (RNI). This assay was analogous to that carried out for ROS determination. This RNI assay serves to quantify the nitrosative stress produced by the materials in the bacterial strains. The same inoculum preparation method as in the previous assay was utilized, and it was incubated with the materials at the same concentration and proportion. However, in this case, the assay was conducted using a standard p96 plate. Once the designated incubation period had elapsed, a 1 : 1 mixture of sulphanilamide (2% in 5% v/v HCl) and *N*-(1-naphthyl)ethylenediamine dihydrochloride (0.1% in distilled H_2O) was added to each well. The plate was then incubated for 15 minutes at 37 °C, after which the absorbance was measured at 540 nm. It is important for this assay to consider a calibration line, in which serial dilutions of sodium nitrite ($NaNO_2$) in the range of 100–0.05 μM were made, to which the same reagents were added to the samples and measured in the same way.

2.2.9. Oxidative stress determined using glutathione (GSH). To evaluate the relationship between the level of oxidative stress produced through ROS generation by the nanomaterials studied, glutathione (GSH) a scavenger of ROS was used. The assay was the same described in 2.2.7 section supplemented with 10 μL of a 1 mM GSH solution in PBS.

2.2.10. Biofilm assays: inhibition and eradication. Biofilm growth tests can be carried out in several ways, on the one hand, the inhibition of biofilm formation on a surface can be studied and on the other, the eradication of a biofilm already formed for 24 h on a surface can be studied. The latter is more difficult to treat since eradicating a biofilm which has already formed the matrix is quite complex. In addition, both assays can be performed with two different protocols, on the one hand, there is the p96 plate assay and on the other, the microscope glass assay. With the first one, quantification is possible, therefore, it was the carried out in this study. For this assays it was necessary to prepare an overnight inoculum, the same as that prepared for the previous assay (*e.g.* MIC and MBC) and the materials at a concentration of 2 mg mL^{-1} in DMSO. It is important to consider in all the assays that a control experiment was performed in which the material is replaced by PBS. For the p96 plate inhibition assay, serial dilutions of each material were prepared, resulting in concentrations ranging from 1000 to 8 μg mL^{-1}. An equal volume of inoculum was added to each well, followed by incubation for 18 hours at 37 °C. After the incubation period, the supernatant was removed, and the wells were washed twice with PBS. The biofilms were then stained with crystal violet solution (1% in distilled water) at 37 °C for 20 minutes. Following staining, the wells were washed again with PBS, and the violet crystals were dissolved with alcohol. Absorbance was measured at 595 nm. A similar procedure was employed for the plate eradication assay, with the exception that on the first day, only the inoculum was incubated to allow for biofilm formation. After 24 hours, the biofilms were subjected to an additional 18-hour incubation with the materials. The subsequent washing and measurement protocol remained consistent with that of the inhibition assay.

2.2.11. Hemolytic activity. With this assay it is possible to quantify the percentage of hemolysis that the final materials can produce. To do this, erythrocytes were first separated from a human blood sample preserved with heparin, this was achieved by centrifuging the sample for 10 minutes at 3000 rpm, and then washing with PBS (×3), and finally dispersing them in a concentration of 1% v/v in PBS. In this protocol it is important to consider a positive control with sodium dodecyl sulphate (SDS) and a negative control with PBS. The materials were tested in dispersions at SUBMIC (MIC/5), MIC and SUPRAMIC (MIC × 5) concentrations in PBS. To carry out the assay, the material was incubated with the erythrocytes in a ratio (1 : 1) for 1, 4 and 24 h at 37 °C. After this time, the material was centrifuged at 3000 rpm for 10 minutes and the supernatant was read at 540 nm in the plate reader.

2.2.12. Cell line and cell culture conditions. Cell line used was Hek 293T, which are human embryonic kidney cells, and are widely used in research to test the potential toxicity of materials. The culture medium used is DMEM (Corning® glutagro™) supplemented with 10% fetal bovine serum (FBS, Cytiva, 0.1 μM) and 1% antibiotics (Penicillin Streptomycin, Corning®). The cells were incubated at 37 °C and 5% CO_2 and the medium was changed 2-3 times a week, depending on cell growth. Trypsin (Corning®) was used to lift the cells and change the medium.

2.2.13. MTT ssay. 3500 cells per well were grown in a p96 plate and left to incubate. After 48 hours, the culture medium was replaced by dispersions of the final materials, made from a stock dispersion of 1 mg mL^{-1}, dilutions were made in complete culture medium to achieve a range of concentrations from 500 to 10 μg mL^{-1} and left to incubate for 24 hours. After this time, 20 μL MTT (1 mg mL^{-1}) was added to each well and then incubated for 3 hours for the formazan salts to form. All the medium and rupture the cell membranes with DMSO, were removed bystirring with a pipette. Finally, read with the Allsheng AMR-100 microplate reader at 570 nm.

2.2.14. Resazurin assay. Plating of the cells and incubation of the materials wass carried out as in Section 2.2.13. After this time, all the medium was removed and replaced by a solution of Resazurin (5 μg mL^{-1}) and left to incubate for 30 minutes, after which the samples were excited at 530 nm and their emission measured by fluorescence at 590 nm with the Cary Eclipse fluorescent spectrophotometer.

2.2.15. Statistical analysis. All the assays were performed at least in triplicate in three independent experiments. Data were expressed as means ± SD and analyzed by the Student's *t*-test, $p < 0.05$ was used as the level of statistical significance.

3. Results and discussion

3.1. Results of synthesis and characterization of the silica-based nanostructured materials

The synthesis of different nanostructured materials based on silica such as MSN, SBA and FSP has been carried out by sol–gel method with different surfactants and protocols (MSN and SBA-15), and by hydrothermal method (FSP) observing that the obtained materials had the expected physical and textural properties.[30]

The nanostructured silica-based systems underwent sequential functionalization with various agents. Initially, an amino-containing ligand (AP ligand) was grafted onto the systems at varying proportions following reported procedures,[31] to establish binding sites on both the internal and external surfaces. Subsequently, an EDAC-type reaction[32] was employed, utilizing (3-carboxypropyl)triphenylphosphonium bromide (PPh_3^+), to introduce phosphonium groups aimed at targeting bacterial membranes, facilitating the formation of amide bonds. Finally, a potentially therapeutic organotin(IV) compound (Fig. 1) was incorporated *via* a protonolysis reaction coupled with the elimination of alcohol. Prior to subjecting the materials to bacterial assays, it is crucial to verify the accuracy of both synthesis and subsequent functionalization processes. To ensure this, a range of physico-chemical characterization techniques were employed, as detailed below.

3.1.1. Nitrogen absorption and desorption isotherms (BET). Initial materials (MSN, SBA and FSP) and the final materials (MSN-AP(10)-PPh_3^+-Sn; MSN-AP(1:1)-PPh_3^+-Sn; SBA-AP(10)-PPh_3^+-Sn; FSP-AP(10)-PPh_3^+-Sn) were analyzed by nitrogen adsorption–desorption isotherm. The isotherms obtained using the BET technique provide several information about the surface area, pore and volume size and some other textural properties.

Fig. 2 shows the nitrogen adsorption and desorption isotherms of the initial materials (MSN, SBA and FSP) and the final materials (MSN-AP(10)-PPh_3^+-Sn; MSN-AP(1:1)-PPh_3^+-Sn; SBA-AP(10)-PPh_3^+-Sn; FSP-AP(10)-PPh_3^+-Sn). For the materials based on MSN nanoplatforms, type IV isotherms are observed. These isotherms are characteristic of mesoporous structures, typical of MSN nanoparticles. However, they could also resemble type VI isotherms, indicative of solid materials with very uniform surfaces. A hysteresis cycle (H2) is present in these materials due to nitrogen condensation by capillarity. This cycle indicates that nitrogen easily enters the pores but exits in a more complex fashion, forming a capillary distribution of nitrogen molecules inside the pores. The SBA-based materials also

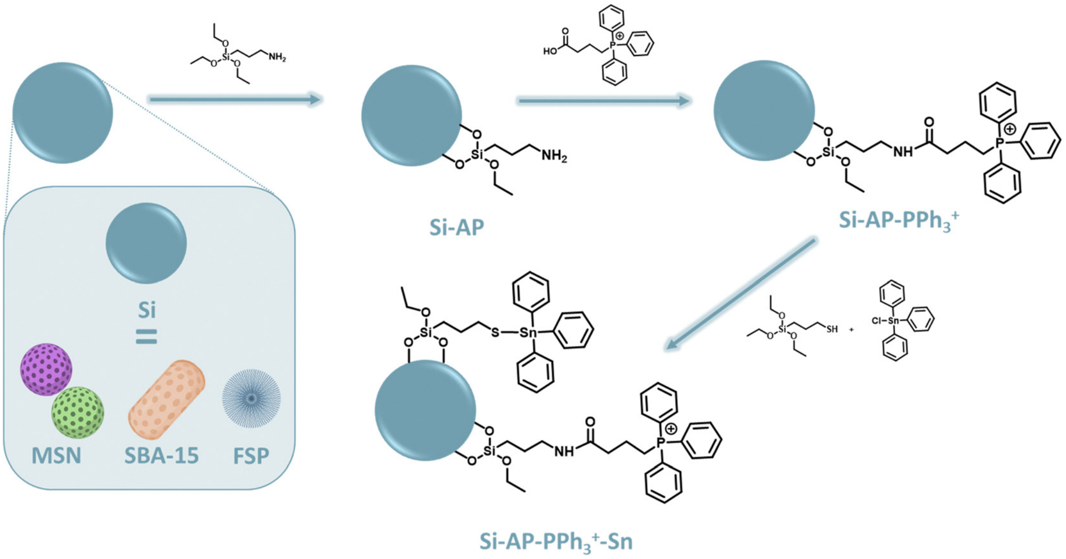

Fig. 1 Scheme of functionalization of the different nanostructured materials proposed for this antibacterial study.

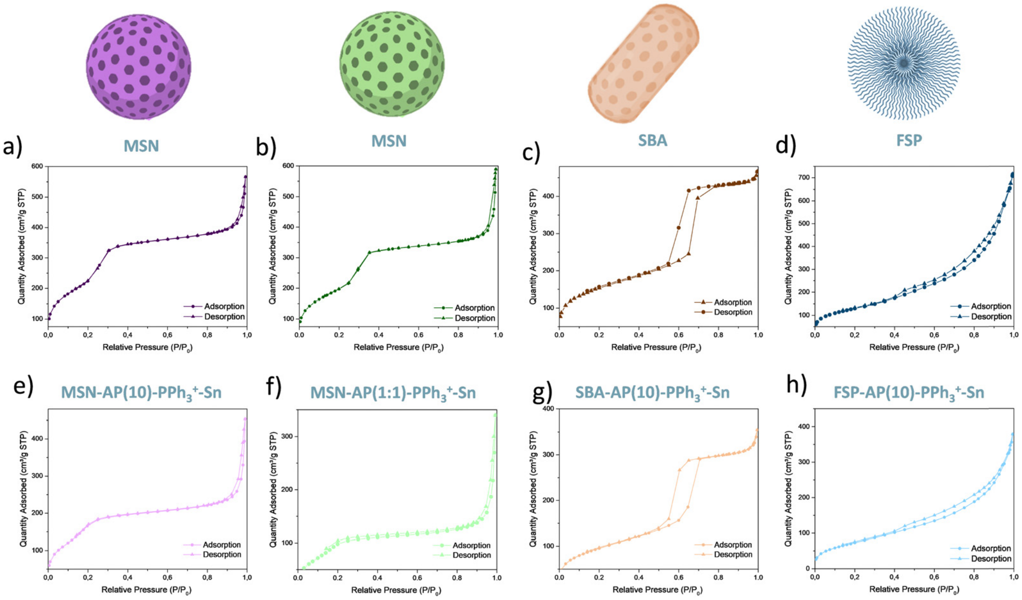

Fig. 2 Nitrogen adsorption–desorption isotherms of starting and final materials: (a) MSN; (b) MSN; (c) SBA; (d) FSP; (e) MSN-AP(10)-PPh$_3$$^+$-Sn; (f) MSN-AP(1:1)-PPh$_3$$^+$-Sn; (g) SBA-AP(10)-PPh$_3$$^+$-Sn; (h) FSP-AP(10)-PPh$_3$$^+$-Sn.

exhibit clear type IV isotherms, characteristic of their mesoporous structure. The H2 hysteresis cycle is visible here as well, resulting from the interaction between the material and nitrogen. In contrast, FSP particles display type III isotherms. This difference arises from the fibrous morphology of the FSP platform, which increases surface area but alters the interaction with nitrogen. The type III isotherm indicates low interaction between the adsorbate and the adsorbent, with nitrogen entering the fibres easily but experiencing capillary condensation upon exit. These observations underscore the distinct adsorption behaviour and structural characteristics of the different silica-based materials.[33–35] Moreover, this technique provides not only isotherm data but also quantitative information on the surface area (m^2 g^{-1}), pore volume (cm^3 g^{-1}), and pore diameter (nm) of the materials (see Table 1). The starting materials (MSN, SBA, and FSP) exhibit large surface areas, ranging from approximately 822 to 473 m^2 g^{-1}. This is significant because a larger surface area facilitates the incorporation of molecules of interest into the nanoplatform's structure.

In the final, functionalized materials (MSN-AP(10)-PPh$_3$$^+$-Sn; MSN-AP(1:1)-PPh$_3$$^+$-Sn; SBA-AP(10)-PPh$_3$$^+$-Sn; FSP-AP(10)-PPh$_3$$^+$-Sn), a noticeable decrease in BET surface area is observed. For instance, the surface area of the highly functionalized (MSN-AP(1:1)-PPh$_3$$^+$-Sn) decreases to 340 m^2 g^{-1}. Additionally, pore size and pore volume are significantly reduced post-functionalization, in some cases by up to 50%.

Table 1 Data obtained in nitrogen adsorption–desorption isotherms using the BET model

Material	BET surface (m^2 g^{-1})	Pore volume (cm^3 g^{-1})	Pore diameter (nm)
MSN	821.71	0.68	3.31
MSN-AP(10)-PPh$_3$$^+$-Sn	646.86	0.45	2.79
MSN	721.12	0.67	3.52
MSN-AP(1:1)-PPh$_3$$^+$-Sn	384.65	0.29	3.00
SBA	551.79	0.69	4.99
SBA-AP(10)-PPh$_3$$^+$-Sn	350.72	0.50	5.96
FSP	472.80	1.01	8.54
FSP-AP(10)-PPh$_3$$^+$-Sn	274.26	0.50	7.36

These observations indicate three key points: firstly, the functionalization has been successful, with clear incorporation of the functional groups into the material; secondly, the functionalization seems to occur throughout the whole material, not just on the external surface but also within the internal pores, explaining the reductions in pore size and volume. Finally, materials with a higher amount of AP ligand show a greater decrease in BET surface area, suggesting a higher incorporation of both the ligand and the other functional molecules. These findings underscore the effectiveness of the functionalization process and its impact on the structural properties of the silica-based materials.

3.1.2. Transmission electron microscopy (TEM).

The size, morphology and distribution of the nanostructured materials is very important to determine their behaviour in biological studies. For example, previous studies by different research groups have shown that the size and morphology of the starting vehicle can play an important role in their interaction with bacteria.[36] Fig. 3 shows the transmission electron microscopy images of the non-functionalized and the loaded systems.

The MSN-based materials (namely, MSN, MSN-AP(10)-PPh$_3$$^+$-Sn and MSN-AP(1:1)-PPh$_3$$^+$-Sn) show a quasi-spherical morphology with size between 70–90 nm and an ordered hexagonal distribution of pores, as expected when compared with other similar materials.[30] In the case of the SBA systems, materials SBA and SBA-AP(10)-PPh$_3$$^+$-Sn materials show a wide rod-like morphology with an elongated dimension. The materials are larger with a particle size distribution of 903.56 nm in length

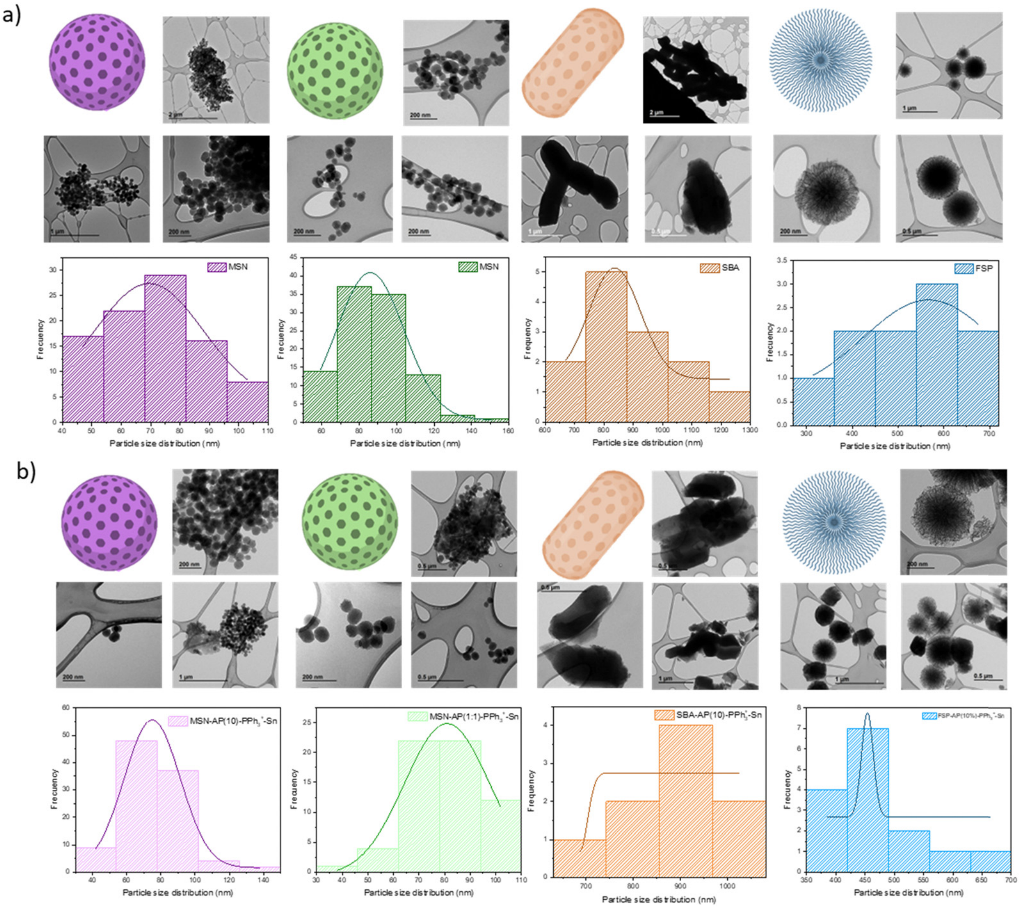

Fig. 3 Images obtained by TEM and representative scheme of size distribution for: (a) starting materials MSN (n = 92), MSN (n = 102), SBA (n = 13) and FSP (n = 10); (b) final materials MSN-AP(10)-PPh$_3^+$-Sn (n = 100); MSN-AP(1:1)-PPh$_3^+$-Sn (n = 61); SBA-AP(10)-PPh$_3^+$-Sn (n = 9); FSP-AP(10)-PPh$_3^+$-Sn (n = 15).

and 691.26 in width, although with a similar hexagonal pore distribution. Both the morphology, particle size and porous arrangement agree with other published SBA-15 materials.

Finally, for the fibrous particles, *i.e.*, FSP and FSP-AP(10)-PPh$_3^+$-Sn, a spherical particle morphology composed of symmetrical fibres is observed. These particles have an intermediate size between MSN and SBA, with average sizes of approximately 500 nm. Quantitative data were obtained using the ImageJ program to generate Gaussian distributions and numerical values of the mean particle size, as shown in Table 2.[37] Additionally, scanning electron microscopy (SEM) was used for the SBA-based materials to observe their distribution and morphology in general. The SEM images can be seen in Fig. S1 (ESI†).

Table 2 Particle size distribution of the studied nanostructured materials obtained by analyzing TEM images using the ImageJ software

Material	Particle size (nm)
MSN	71.20 ± 16.29
MSN-AP(10)-PPh$_3^+$-Sn	77.01 ± 17.76
MSN	87.26 ± 18.30
MSN-AP(1:1)-PPh$_3^+$-Sn	79.69 ± 14.87
SBA	902.71 ± 143.65
SBA-AP(10)-PPh$_3^+$-Sn	904.41 ± 97.02
FSP	513.08 ± 115.20
FSP-AP(10)-PPh$_3^+$-Sn	466.04 ± 74.49

3.1.3. Infrared spectrum (FT-IR). Covalent functionalization was confirmed through FT-IR spectroscopic analysis, yielding distinct spectra showcasing new bands corresponding to bond vibrations upon the material's functionalization with various compounds (AP, PPh$_3^+$, Sn) (Fig. S2, ESI†). Initially, spectra of MSN, SBA and FSP showed characteristic bands attributed to the vibrations of (O–H) and (Si–OH) bonds at around 3500 cm^{-1} and additional bands corresponding to (Si–O–Si) bonds were evident around 1100 cm^{-1}. These bands are in line with non-modified MSN, SBA, and FSP materials. Following functionalization with the AP ligand, new bands attributed to (C–H) and (N–H) bond vibrations emerged at *ca.* 2900 cm^{-1} attributed to C–H and N–H vibrations and at 1600 cm^{-1}, corresponding to the hydrocarbon chain of the ligand structure. These bands were further intensified upon functionalization with the PPh$_3^+$ compound. Furthermore, the appearance of (C–C) bond vibrations, originating from the aromatic rings within the ligand structure, was notable at

1500 cm^{-1}. Finally, functionalization with Sn resulted in the emergence of distinctive bands representing (Sn–C) bond vibrations at *ca.* 750 cm^{-1}, accompanied by intensified bands at 1000 cm^{-1}.[38]

3.1.4. Ultraviolet visible spectroscopy (UV-Vis). Ultraviolet-visible spectroscopy served as another pivotal technique for assessing the successful derivatization of the nanomaterials. As anticipated, the UV-Vis spectra exhibited similarities across all initial vehicles, despite variations in morphology, owing to their common chemical foundation rooted in silica (Fig. S3, ESI†).

In this regard, silica-based materials displayed a distinct band at approximately 250 nm following functionalization with the AP ligand, attributed to the integration of the organic fragment. Subsequent incorporation of the PPh_3^+ moiety led to an intensification of this peak, with further enhancement observed upon the introduction of the organotin(IV) complex. Notably, the latter transformation also manifested a characteristic peak around 270 nm, indicative of the presence of the metal-containing fragment.[39]

3.1.5. Powder X-ray diffraction (XRD). Powder X-ray diffraction (XRD) studies provided valuable insights into the structural alterations resulting from functionalization. In the XRD spectra of the non-functionalized silica-based materials MSN and SBA (Fig. 4 and Table 3), the mesoscopic order of the porous structures was evident at low angles, with diffractograms exhibiting characteristic peaks corresponding to the Miller planes [100], [110], and [200] at 2θ values of 2.38, 4.13, and 4.75 in MSN, and 0.96, 1.66, and 1.92 in SBA, affirming a hexagonal porous arrangement within these systems. Conversely, in FSP materials characterized by a fibrous porous arrangement, intense diffraction peaks were not observed, as anticipated. Following the incorporation of various fragments into the nanomaterials, a reduction in the intensity of signals corresponding to the [100] plane was noted, with instances where signals for the [110] and [200] planes disappeared entirely. This diminished intensity can be attributed to the obscuring of scattering points after functionalization, serving as further confirmation of successful incorporation of the different agents. Additionally, in some cases, slight shifts in peaks were observed, indicative of minor alterations in pore size subsequent to functionalization.[40]

Table 3 XRD data of MSN, MSN-AP(10)-PPh_3^+-Sn, MSN-AP(1:1)-PPh_3^+-Sn, SBA, SBA-AP(10)-PPh_3^+-Sn; FSP and FSP-AP(10)-PPh_3^+-Sn

Material	(*hkl*)	2θ (°)	d_{hkl} (Å)
MSN	100	2.38	37.05
	110	4.13	21.38
	200	4.75	18.60
MSN-AP(10)-PPh_3^+-Sn	100	2.37	37.20
	110	4.13	21.38
	200	4.76	18.57
MSN	100	2.28	38.35
	110	3.92	22.53
	200	4.54	19.44
MSN-AP(1:1)-PPh_3^+-Sn	100	2.28	38.66
	200	4.48	19.73
SBA	100	0.96	92.34
	110	1.66	53.30
	200	1.92	45.92
SBA-AP(10)-PPh_3^+-Sn	100	0.96	91.67
	110	1.67	52.97
	200	1.93	45.70
FSP	—	1.70	51.92
FSP-AP(10)-PPh_3^+-Sn	—	1.22	71.79

3.1.6. Quantification of targeting and therapeutic functionalization by TG and/or ICP. With the techniques employed so

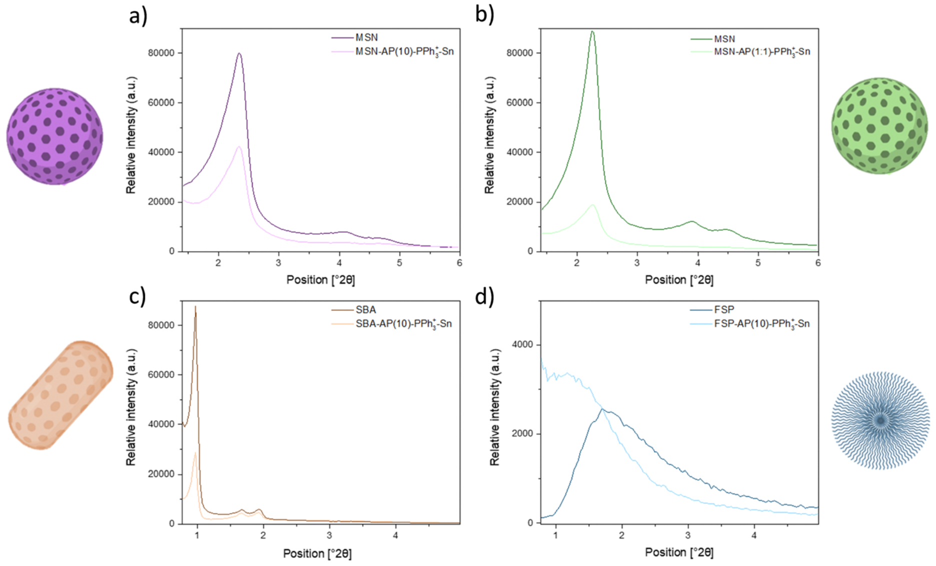

Fig. 4 Powder X-ray diffractograms obtained for all studied materials: (a) MSN and MSN-AP(10)-PPh_3^+-Sn; (b) MSN and MSN-AP(1:1)-PPh_3^+-Sn; (c) SBA and SBA-AP(10)-PPh_3^+-Sn; (d) FSP and FSP-AP(10)-PPh_3^+-Sn.

Table 4 Data obtained by TG (for AP) and ICP-MS (for P and/or Sn)

Material	AP weight (%)	AP mmol g^{-1}	P (%)	Sn (%)
MSN-AP(10)	5.41	0.28	—	—
MSN-AP(1:1)	16.59	0.86	—	—
SBA-AP(10)	6.77	0.35	—	—
FSP-AP(10)	7.00	0.36	—	—
MSN-AP(10)-PPh_3^+	—	—	0.045 ± 0.001	—
MSN-AP(1:1)-PPh_3^+	—	—	0.101 ± 0.001	—
SBA-AP(10)-PPh_3^+	—	—	0.047 ± 0.001	—
FSP-AP(10)-PPh_3^+	—	—	0.043 ± 0.001	—
MSN-AP(10)-PPh_3^+-Sn	—	—	not analyzed	1.802 ± 0.001
MSN-AP(1:1)-PPh_3^+-Sn	—	—	not analyzed	1.681 ± 0.001
SBA-AP(10)-PPh_3^+-Sn	—	—	not analyzed	1.672 ± 0.001
FSP-AP(10)-PPh_3^+-Sn	—	—	not analyzed	1.905 ± 0.014

far, we have gathered data on the morphology and successful functionalization of the synthesized nanomaterials. However, quantifying the amount of ligand or molecule incorporated into each platform requires additional techniques. For this purpose, we utilized thermogravimetry (TG) and inductively coupled plasma mass spectrometry (ICP-MS).

TG was used to quantify the amount of AP ligand in the MSN-AP(10), MSN-AP(1:1), SBA-AP(10), and FSP-AP(10) materials, and to assess their thermal stability. ICP-MS was employed to accurately quantify the number and quantity of specific elements in the samples. The materials were digested in 1 mg mL^{-1} KOH (2 M) and agitated for 48 hours before filtration and measurement. Using ICP-MS, we measured the phosphorus content in MSN-AP(10)-PPh_3^+, MSN-AP(1:1)-PPh_3^+, SBA-AP(10)-PPh_3^+ and FSP-AP(10)-PPh_3^+ to determine the amount of PPh_3^+ incorporated. Similarly, the tin content in MSN-AP(10)-PPh_3^+-Sn, MSN-AP(1:1)-PPh_3^+-Sn, SBA-AP(10)-PPh_3^+-Sn and FSP-AP(10)-PPh_3^+-Sn was quantified, which is crucial for evaluating the antibacterial potential, as tin acts as the cytotoxic agent in these nanostructures.

Table 4 shows the TG data for materials functionalized with AP. For a theoretical 10% ligand incorporation, the actual amount ranges between 6% and 7%, with the highest being in the FSP nanostructure. For the material with a theoretical 1 : 1 ligand ratio, the actual amount is about 17%, roughly three times higher than the previous ones. Although these values are below the theoretical amount, they are consistent with previous results from our group.[41] The free amino groups on the surface serve as anchor points for the targeting agent (PPh_3^+), as confirmed by TG measurements Fig. S4 (ESI†). Column 3 of Table 4 presents the phosphorus measurements by ICP-MS, indicating the actual amount of PPh_3^+ in each nanomaterial. Although the values are approximately ten times lower than those of AP, they should suffice for functionality, which will be verified in subsequent antibacterial tests. Additionally, materials with more AP ligand (*e.g.*, MSN-AP(1:1)) contain more triphenylphosphonium salt, corroborating that the NH_2 groups of the ligand are covalent binding points to the silica. Finally, using ICP-MS, we quantified the tin content in the final materials. The synthesis of the tin complex (detailed in Section 2.1.7) ensures that the metal content is independent of the initial functionalization amount, although highly functionalized silica complicates further incorporation. Functionalization values are close to 2%, with the highly functionalized MSN (MSN-AP(1:1)-PPh_3^+-Sn) having 0.12% less tin than the less functionalized MSN (MSN-AP(10)-PPh_3^+-Sn). Notably, the FSP nanoplatform contains the highest amount of metal at *ca.* 1.91%, likely due to its fibrous pore morphology facilitating molecule incorporation. This comprehensive quantification confirms the effective functionalization of the nanomaterials and sets the stage for evaluating their antibacterial properties.

3.2. Results of biological studies

3.2.1. Sn release study in physiologic medium. Taking advantage of the quantification of Sn metal by ICP-MS technique, a metal release assay was performed to evaluate the stability of the material and its behaviour in a physiological suspension over time.

Fig. 5 illustrates the percentage of Sn released by each material over time, relative to the percentage of Sn functionalized in the material (as detailed in Table 4). All materials exhibited a gradual release of tin, reaching a maximum release at 4 hours and stabilizing by 24 hours. The metal release values remained below 3% of the total Sn functionalized in each material, which is in line with similar systems published in our group. This low release rate is attributed to the non-classical functionalization of the nanoplatforms, where all

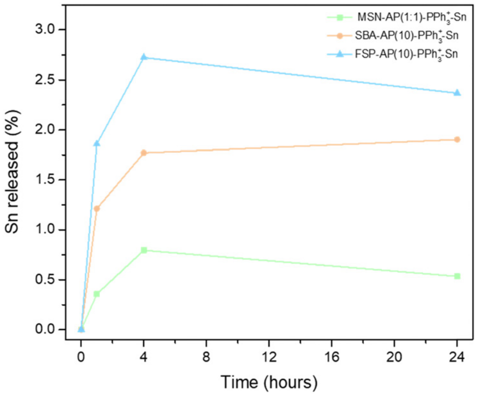

Fig. 5 Experimental quantity of Sn released (% of the loaded Sn) in simulated biological medium, measured in ICP, from the materials: MSN-AP(1:1)-PPh_3^+-Sn; SBA-AP(10)-PPh_3^+-Sn; FSP-AP(10)-PPh_3^+-Sn.

molecules are covalently incorporated. Consequently, the material functions cohesively in the biological environment without needing to release the cytotoxic agent. In particular, the FSP-type silica showed rapid metal release, possibly attributable to its fibrous structure, which may provide a more accessible environment for release compared to materials with hexagonal pores and long channels.

3.2.2. Diffusion test. The first antimicrobial activity test employed was the diffusion test, designed to assess how the materials deposited in the wells of a Petri dish, seeded with a bacterial strain, create a bacteria-free zone around the well. A well containing PBS served as a negative diffusion control, while a ciprofloxacin disk acted as a positive control, given its efficacy against the bacterial strains under investigation.

As depicted in Fig. 6 the final materials exhibited diffusion halos in the *S. aureus* strain, while the starting and intermediate materials did not. This observation underscores the significant role of the cytotoxic agent, specifically the organotin(IV) complex, in combating this bacterial strain. Qualitative data, measured from the inhibition halo of each material (Table 5), revealed similar halos across the materials, resulting in halo values between 18 and 20 mm. Notably, no difference in activity was observed between MSN-AP(10) and MSN-AP(1:1),

Table 5 Inhibition halo obtained by the agar diffusion test with all materials in the *S. aureus* strain

Material	Diffusion (mm)
PBS	8 ± 1
Ciprofloxacin	29 ± 1
MSN	8 ± 1
MSN	8 ± 1
SBA	8 ± 1
FSP	8 ± 1
PBS	8 ± 1
Ciprofloxacin	30 ± 1
MSN-AP(10)	8 ± 1
MSN-AP(1:1)	8 ± 1
SBA-AP(10)	8 ± 1
FSP-AP(10)	8 ± 1
PBS	8 ± 1
Ciprofloxacin	29 ± 1
MSN-AP(10)-PPh_3^+	8 ± 1
MSN-AP(1:1)-PPh_3^+	8 ± 1
SBA-AP(10)-PPh_3^+	8 ± 1
FSP-AP(10)-PPh_3^+	8 ± 1
PBS	8 ± 1
Ciprofloxacin	30 ± 1
MSN-AP(10)-PPh_3^+-Sn	18 ± 1
MSN-AP(1:1)-PPh_3^+-Sn	18 ± 1
SBA-AP(10)-PPh_3^+-Sn	20 ± 1
FSP-AP(10)-PPh_3^+-Sn	20 ± 1

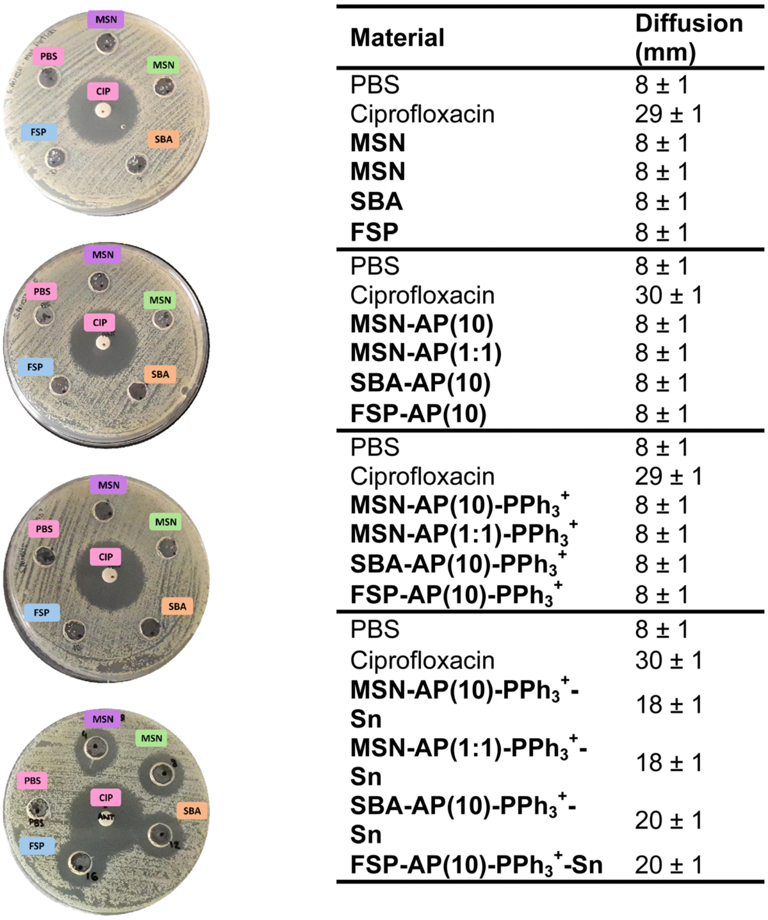

Material	Diffusion (mm)
PBS	8 ± 1
Ciprofloxacin	29 ± 1
MSN	8 ± 1
MSN	8 ± 1
SBA	8 ± 1
FSP	8 ± 1
PBS	8 ± 1
Ciprofloxacin	30 ± 1
MSN-AP(10)	8 ± 1
MSN-AP(1:1)	8 ± 1
SBA-AP(10)	8 ± 1
FSP-AP(10)	8 ± 1
PBS	8 ± 1
Ciprofloxacin	29 ± 1
MSN-AP(10)-PPh_3^+	8 ± 1
MSN-AP(1:1)-PPh_3^+	8 ± 1
SBA-AP(10)-PPh_3^+	8 ± 1
FSP-AP(10)-PPh_3^+	8 ± 1
PBS	8 ± 1
Ciprofloxacin	30 ± 1
MSN-AP(10)-PPh_3^+-Sn	18 ± 1
MSN-AP(1:1)-PPh_3^+-Sn	18 ± 1
SBA-AP(10)-PPh_3^+-Sn	20 ± 1
FSP-AP(10)-PPh_3^+-Sn	20 ± 1

Fig. 6 Images obtained from the diffusion test with all materials in the *S. aureus* strain.

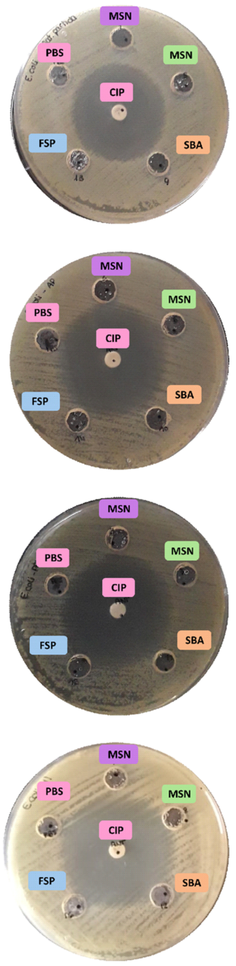

Material	Diffusion (mm)
PBS	8 ± 1
Ciprofloxacin	37 ± 1
MSN	8 ± 1
MSN	8 ± 1
SBA	8 ± 1
FSP	8 ± 1
PBS	8 ± 1
Ciprofloxacin	40 ± 1
MSN-AP(10)	8 ± 1
MSN-AP(1:1)	8 ± 1
SBA-AP(10)	8 ± 1
FSP-AP(10)	8 ± 1
PBS	8 ± 1
Ciprofloxacin	42 ± 1
MSN-AP(10)-PPh_3^+	8 ± 1
MSN-AP(1:1)-PPh_3^+	8 ± 1
SBA-AP(10)-PPh_3^+	8 ± 1
FSP-AP(10)-PPh_3^+	8 ± 1
PBS	8 ± 1
Ciprofloxacin	44 ± 1
MSN-AP(10)-PPh_3^+-Sn	8 ± 1
MSN-AP(1:1)-PPh_3^+-Sn	8 ± 1
SBA-AP(10)-PPh_3^+-Sn	8 ± 1
FSP-AP(10)-PPh_3^+-Sn	8 ± 1

Fig. 7 Images obtained from the diffusion test with all materials in the *E. coli* strain.

suggesting that the ligand quantity did not impact material activity in this assay.

Conversely, with the *E. coli* strain (Fig. 7 and Table 6) none of the materials displayed significant inhibition halos. However, this absence does not preclude potential activity of the final materials against this strain.

With these results, subsequent bacterial activity tests were conducted exclusively with the final materials, as the starting and intermediate materials demonstrated no activity against either studied strain.

3.2.3. Minimum inhibitory concentration (MIC) and minimum bactericidal concentration (MBC). Following the diffusion assay, the final materials were carefully selected for minimum inhibitory concentration (MIC) and minimum bactericidal concentration (MBC) assays against *S. aureus* and *E. coli* strains. After incubation with the final materials, images Fig. S5 (ESI†) were captured, and staining with Resazurin facilitated the determination of MIC values for each material against both bacterial strains, as summarized in Table 7.

Table 7 presents the antibacterial activity data for the bacterial strain *S. aureus*. The MSN-based materials show identical MIC (minimum inhibitory concentration) and MBC (minimum bactericidal concentration) values, at 62.50 and 125.00 μg mL^{-1}, respectively. However, the MSN-AP(1:1)-PPh_3^+-Sn has approximately 0.1% less metal content compared to MSN-AP(10)-PPh_3^+-Sn.

For the SBA-based materials, the MIC value is half that of the MSN materials, while the MBC value is double. These values correlate proportionally with the metal content. In the FSP-based nanomaterials, MIC values are four times lower and MBC values are halved compared to the MSN materials, which also aligns with the amount of incorporated metal.

The fourth column of Table 7 shows the relationship between MIC and MBC values. The MSN-based materials exhibit bactericidal activity despite higher MIC and MBC values. In contrast, the SBA and FSP materials display bacteriostatic activity, although their MIC values are somewhat lower.

The second part of Table 7 summarizes the results for the *E. coli* bacterial strain. All materials exhibit the same MIC value, with the FSP material containing the highest amount of tin, as confirmed by ICP-MS measurements. The MBC values for SBA are twice as high in both material and metal content. Overall, all materials demonstrate bactericidal activity against *E. coli*.

Table 6 Inhibition halo obtained by the agar diffusion test with all materials in the *E. coli* strain

Material	Diffusion (mm)
PBS	8 ± 1
Ciprofloxacin	37 ± 1
MSN	8 ± 1
MSN	8 ± 1
SBA	8 ± 1
FSP	8 ± 1
PBS	8 ± 1
Ciprofloxacin	40 ± 1
MSN-AP(10)	8 ± 1
MSN-AP(1:1)	8 ± 1
SBA-AP(10)	8 ± 1
FSP-AP(10)	8 ± 1
PBS	8 ± 1
Ciprofloxacin	42 ± 1
MSN-AP(10)-PPh_3^+	8 ± 1
MSN-AP(1:1)-PPh_3^+	8 ± 1
SBA-AP(10)-PPh_3^+	8 ± 1
FSP-AP(10)-PPh_3^+	8 ± 1
PBS	8 ± 1
Ciprofloxacin	44 ± 1
MSN-AP(10)-PPh_3^+-Sn	8 ± 1
MSN-AP(1:1)-PPh_3^+-Sn	8 ± 1
SBA-AP(10)-PPh_3^+-Sn	8 ± 1
FSP-AP(10)-PPh_3^+-Sn	8 ± 1

Comparing the results for both bacterial strains, we observe that the values for *E. coli* are similar to those for MSN and higher for SBA and FSP. However, all tested materials show bactericidal activity, highlighting their potential effectiveness against both bacterial strains. Given the potential antibacterial treatment implications, bactericidal activity is considered more advantageous. These results suggest promising potential for nanomaterial-based treatments and imply that PPh_3^+ primarily influences Gram-negative bacteria.

Analyzing the amount of PPh_3^+ present in each material, one can easily see that there are no significant differences in the results obtained with the MSN material containing 0.045%, compared to that of the systems containing 0.101%. In this context, one can conclude that with an amount of 0.043% of PPh_3^+ incorporated in the final material FSP-AP(10)-PPh_3^+-Sn seems to be sufficient to prove its potential targeting by the increase of the activity, especially against the bacterial strain *E. coli*.

For the well-known silver nanoparticles, commonly used as antibacterial agents, the MIC values are approximately 125 μg mL^{-1} and the MBC values are 250 μg mL^{-1}. These values are up to 100 times higher, indicating a lower antibacterial activity of silver nanoparticles compared to the Sn-containing materials studied, when considering the amount of metal, which is the cytotoxic agent in each silica-based material.[42]

3.2.4. Death curves. A bacterial death curve was constructed to monitor bacterial death over time, focusing on materials MSN-AP(1:1)-PPh_3^+-Sn, SBA-AP(10)-PPh_3^+-Sn, and FSP-AP(10)-PPh_3^+-Sn. These materials were selected based on previous findings indicating that the quantity of AP does not impact nanomaterial activity. As illustrated in Fig. 8, both bacterial strains exhibited a notable decrease in colony forming units (CFU) over time, with a slight increase observed after 1 hour but reaching their nadir at 4 hours, notably with a more pronounced decline observed in the *E. coli* strain. These results can be compared with those from the simulated biological medium release assay (Fig. 5), elucidating a direct correlation between bacterial death and metal release into the medium. Notably, all data acquired during this assay were benchmarked against a growth control, wherein bacteria were incubated for the same duration sans material, revealing a considerable increase in bacterial growth over time. These findings hold significance for quantifying future cell metabolism assays accurately, as they will be recalibrated based on CFU counts obtained at each hour, thus providing a realistic assessment of bacterial response to the materials over time.

3.2.5. Oxidative stress (ROS). Examining the metabolic response of both bacterial strains to the materials was imperative, utilizing the same materials as in the preceding assays. Among the potential metabolic pathways, oxidative stress stands out, characterized by the formation and quantification of reactive oxygen species (ROS) *via* fluorometry.

Following bacterial incubation with the materials for varying durations, fluorescence data were collected. To accurately quantify ROS production by live bacteria at each incubation point, these fluorescence data were juxtaposed with CFU mL^{-1} data obtained from the previous death curve test. Fig. 9 illustrates the percentage of ROS at each hour of incubation. Remarkably, a notable percentage of ROS was detected across all materials, with an observable increase at the 4-hour mark of incubation. Quantitatively, it is evident that at 4 hours, the ROS value in the SBA-AP(10)-PPh_3^+-Sn material increases by 10^{18}%

Table 7 Quantitative data obtained from MIC and MBC assays, and conclusion obtained from the ratio of both assays

Material	MIC [Sn] (μg mL^{-1})	MBC [Sn] (μg mL^{-1})	Conclusion
S. aureus (ATCC 29213)			
MSN-AP(10)-PPh_3^+-Sn	62.50 [1.13]	125.00 [2.25]	Bactericide
MSN-AP(1:1)-PPh_3^+-Sn	62.50 [1.01]	125.00 [2.10]	Bactericide
SBA-AP(10)-PPh_3^+-Sn	31.25 [0.52]	250.00 [4.18]	Bacteriostatic
FSP-AP(10)-PPh_3^+-Sn	15.63 [0.30]	62.50 [1.22]	Bacteriostatic
E. coli (ATCC 25922)			
MSN-AP(10)-PPh_3^+-Sn	250.00 [4.51]	250.00 [4.51]	Bactericide
MSN-AP(1:1)-PPh_3^+-Sn	250.00 [4.20]	250.00 [4.20]	Bactericide
SBA-AP(10)-PPh_3^+-Sn	250.00 [4.18]	500.00 [8.36]	Bactericide
FSP-AP(10)-PPh_3^+-Sn	250.00 [4.88]	250.00 [4.88]	Bactericide

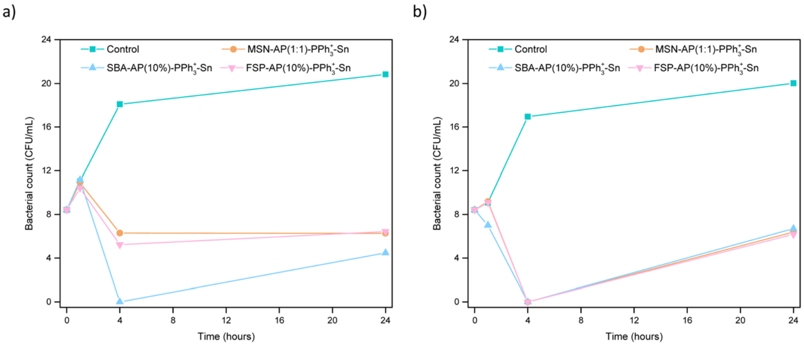

Fig. 8 Plots of death curves, represented in CFU mL^{-1} *versus* time: (a) *S. aureus*; (b) *E. coli*.

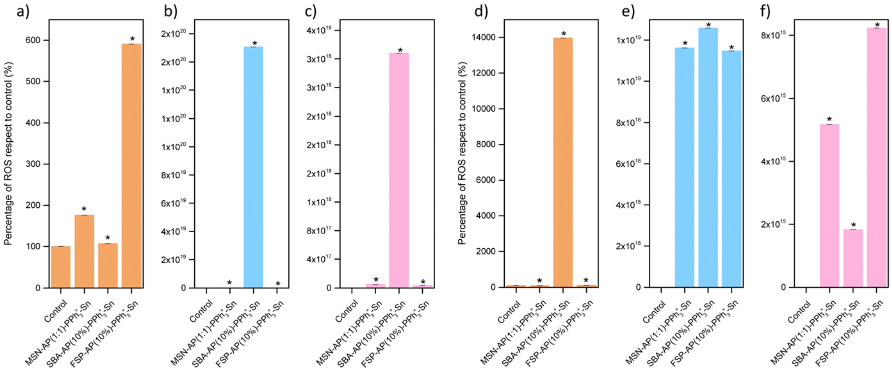

Fig. 9 Percentages of ROS obtained after incubation with the materials in bacteria: (a) *S. aureus* 1 h; (b) *S. aureus* 4 h; (c) *S. aureus* 24 h; (d) *E. coli* 1 h; (e) *E. coli* 4 h; (f) *E. coli* 24 h (* = $p < 0.05$).

compared to the value obtained at 1 hour, occurring in both bacterial strains. While significant ROS values are observed in all materials across all time points, the highest values at 4 hours are associated with the SBA-based material. Conversely, at 24 hours, the highest ROS values in *E. coli* are found in the FSP-based material. These findings indicate that the morphology of the starting material significantly impacts both antibacterial activity and metabolism. Notably, the ROS values reported here surpass those found in the literature for similar materials.[36]

These results are in concordance with those of the death curve test, wherein a noticeable change, particularly in the *E. coli* strain, was observed at the 4-hour experiment. This synchronous change in ROS production and bacterial death underscores the significance of oxidative stress as a potential mechanism underlying the antibacterial activity of the materials (for an additional scaling of Fig. 9 with respect to the highest ROS concentration, see Fig. S6 of ESI†).

3.2.6. Nitrosative stress (RNI).

Another significant metabolic pathway in bacteria involves nitrosative stress induced by nitric oxide formation. This assay, analogously to the ROS analysis, relies on colorimetry to quantify the percentage of reactive nitrogen intermediates (RNI) resulting from nitric oxide formation. To compute the percentage of RNI, a calibration curve established earlier is utilized, while absorbance values are determined based on results from the death curve assay and is a very interesting tool to understand the mechanistic insights of the use of nanoparticles against bacteria.[43]

Following incubation of the materials for various durations and subsequent staining with reagents, Fig. 10 presents graphs depicting the percentage of RNI formed. These graphs reveal a trend similar to that observed in the ROS assays, suggesting a direct relationship between metabolic activity, whether oxidative or nitrosative stress, and the death curves obtained, which correspond to colony formation at each time point studied. Consistent with the previous observations, the material with the highest RNI values is SBA-AP(10)-PPh$_3^+$-Sn, showing a 10^{18}% increase in metabolic activity at 4 hours (for an additional scaling of Fig. 10 with respect to the highest RNI concentration, see Fig. S7 of ESI†).

Notably, the percentage of RNI follows a trend similar to that of ROS, albeit with slightly lower values. Consequently, it can be inferred that the primary metabolic pathway in both bacterial strains when exposed to MSN-AP(1:1)-PPh$_3^+$-Sn, SBA-AP(10)-PPh$_3^+$-Sn, and FSP-AP(10)-PPh$_3^+$-Sn materials predominantly involves the generation of ROS.

Furthermore, to ascertain the predominant metabolic pathway in each bacterial strain, Table 8 presents the ROS and RNI values obtained in each test, expressed as a percentage, along with the ROS/RNI ratio. Analysis of this ratio reveals that, across

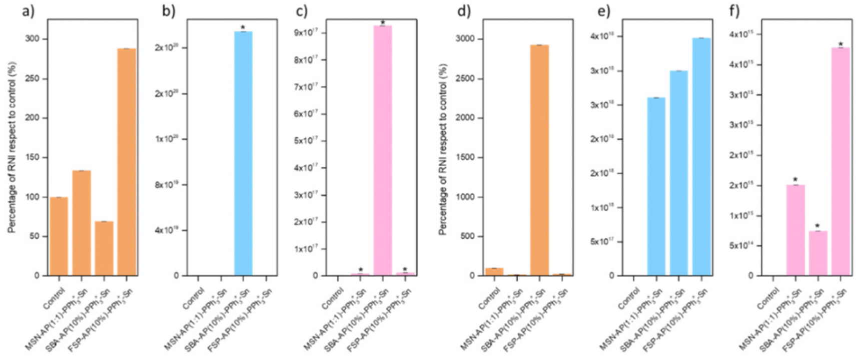

Fig. 10 Percentages of RNI obtained after incubation with the materials in the strains: (a) *S. aureus* 1 h; (b) *S. aureus* 4 h; (c) *S. aureus* 24 h; (d) *E. coli* 1 h; (e) *E. coli* 4 h; (f) *E. coli* 24 h (* = $p < 0.05$).

Table 8 Quantitative data obtained from ROS and RNI assays, and conclusion obtained from the ratio of both assays

Material	Time (h)	ROS (%)	RNI (%)	ROS/RNI
S. aureus ATCC 29213				
MSN-AP(1:1)-PPh$_3$$^+$-Sn	1	1.76×10^2	1.34×10^2	1.32
	4	1.07×10^2	6.89×10^1	1.55
	24	5.91×10^2	2.88×10^2	2.05
SBA-AP(10)-PPh$_3$$^+$-Sn	1	8.98×10^{13}	3.02×10^{13}	2.97
	4	1.71×10^{20}	2.14×10^{20}	0.80
	24	1.09×10^{15}	6.67×10^{14}	1.63
FSP-AP(10)-PPh$_3$$^+$-Sn	1	5.21×10^{16}	8.21×10^{15}	6.35
	4	3.28×10^{18}	9.27×10^{17}	3.54
	24	3.53×10^{16}	1.07×10^{16}	3.29
E. coli ATCC 25922				
MSN-AP(1:1)-PPh$_3$$^+$-Sn	1	9.20×10^1	1.80×10^1	5.11
	4	1.40×10^4	2.92×10^3	4.78
	24	1.11×10^2	2.22×10^1	5.01
SBA-AP(10)-PPh$_3$$^+$-Sn	1	1.16×10^{19}	2.61×10^{18}	4.46
	4	1.26×10^{19}	3.00×10^{18}	4.19
	24	1.15×10^{19}	3.48×10^{18}	3.30
FSP-AP(10)-PPh$_3$$^+$-Sn	1	5.17×10^{15}	1.51×10^{15}	3.41
	4	1.83×10^{15}	7.43×10^{14}	2.46
	24	8.23×10^{15}	3.78×10^{15}	2.17

both strains and all final materials, the predominant pathway is the generation of reactive oxygen species. These findings are consistent with literature, where ROS generation is commonly observed as the primary route in most cases.[44] Additionally, it is notable that in the case of materials MSN-AP(1:1)-PPh$_3$$^+$-Sn and SBA-AP(10)-PPh$_3$$^+$-Sn tested against the *E. coli* strain, higher values were recorded, indicating a greater generation of ROS in the negative strain. This observation underscores the enhanced ROS production in *E. coli* compared to *S. aureus*, further supporting the primary role of ROS in the antibacterial mechanism of these materials. The values obtained in these bacterial metabolism studies cannot be directly compared with those in the literature, as the use of tin-functionalized silicon nanomaterials as antibacterials has not been previously studied. This represents a promising new direction for future research. In the study by Ugalde-Arbizu *et al.*[26] where MSN-type silica materials were examined, the maximum ROS values reported were 60% at 4 hours. In contrast, the significantly higher ROS values obtained in this work highlight the enhanced antibacterial activity of the final materials as plausible coatings.

3.2.7. Oxidative stress determined using GSH.

GSH can be oxidized spontaneously in the presence of ROS, which can neutralize the GSH's antioxidant capacity. Table 9 and Fig. S8 of ESI† summarize the measured levels of ROS after the preincubation of bacterial cells with the nanomaterials without GSH and supplemented with GSH. It is known that ROS can increase the sensitivity of bacteria to antimicrobial agents like gentamycin against *E. coli*.[45] In this context, it is well known that the ROS scavengers can target a particular species, or all the species produced, as GSH is a tripeptide of low size and good potential to interact with different systems, therefore, acting as a general redox ROS scavenger.[46]

From the present study, one can infer that there was an increase in ROS production after bacterial treatment with the materials, compared to untreated (control) bacteria. In addition, the enhanced ROS generation by the nanomaterials was

Table 9 Percentage of reduction of intracellular ROS with GSH in *S. aureus* and *E. coli*

Material	Time (h)	% of Reduction in ROS levels by GSH
S. aureus ATCC 29213		
MSN-AP(1:1)-PPh$_3$$^+$-Sn	1	14.6
	4	2.6
	24	18.4
SBA-AP(10)-PPh$_3$$^+$-Sn	1	44.2
	4	60.0
	24	14.0
FSP-AP(10)-PPh$_3$$^+$-Sn	1	61.1
	4	32.6
	24	32.9
E. coli ATCC 25922		
MSN-AP(1:1)-PPh$_3$$^+$-Sn	1	12.7
	4	42.3
	24	0.0
SBA-AP(10)-PPh$_3$$^+$-Sn	1	21.4
	4	10.3
	24	11.9
FSP-AP(10)-PPh$_3$$^+$-Sn	1	30.0
	4	26.5
	24	26.7

also confirmed by intracellular ROS levels measurements even in the presence of GSH.

From the obtained results it is clear that GSH protect different cellular components by slightly neutralizing ROS. Table 9 shows that the addition of GSH reduced the ROS levels at all times evaluated, including up to 60% at the maximum ROS in *S. aureus* and 42% in *E. coli*. However, there were very interesting results observed for some of the materials, for example the system MSN-AP(1:1)-PPh_3^+-Sn showed to generate persistent ROS, as the reduction of ROS levels by GSH were between only *ca.* 3–18% after 1, 4 or 24 hours in the case of *S. aureus* and even of 0% after 24 hours in the case of *E. coli* strains.

These results indicate that increased ROS production and the relatively low reduction of the ROS levels by GSH when treating the bacterial strains with MSN-AP(1:1)-PPh_3^+-Sn greatly contributes to the impact of the nanomaterials on *S. aureus* and *E. coli* colonies and their potential viability.

3.2.8. Biofilm assays: inhibition and eradication. Fig. 11 illustrates the percentage inhibition of biofilm formation in both *S. aureus* (top) and *E. coli* (bottom) strains resulting from incubation with the final materials before biofilm formation occurs. It is evident that the materials exert inhibitory effects on biofilm formation in both strains. Particularly in *S. aureus*, MSN-AP(10)-PPh_3^+-Sn exhibits notable inhibitory activity, achieving over 50% inhibition at higher material concentrations, which is clearly higher than in the case of some other similar materials with metal complexes or metal nanoparticles supported onto silica-based nanostructured systems.[47] In addition, these tin materials present comparable, if not somewhat higher activity than tin oxide nanoparticles.[48]

In *E. coli*, the degree of inhibition correlates closely with material concentration. Conversely, eradicating established biofilms poses a greater challenge, as incubation with the materials occurs after biofilm formation, over a 24-hour period. Despite using lower material concentrations, significant effects of the materials on biofilm eradication are observed. In *S. aureus* (Fig. 12), while materials exhibit less efficacy in eradicating biofilms compared to inhibiting their formation, there is a trend towards increased eradication with higher material concentrations. In *E. coli*, eradication percentages increase with material concentration, except for **SBA-AP(10)-PPh_3^+-Sn**, which shows no activity.

To the best of our knowledge this is the first organotin(IV)-based nanomaterial which shows a good degree of eradication in both *E. coli* and *S. aureus* biofilms, opening up the opportunity to further explore this kind of systems more in detail in preclinical trials in a short-term future.

3.2.9. Hemolysis. The hemolysis assay serves to simulate material behaviour in a medium akin to biological environments, thus offering insights crucial for future *in vivo* assays. In this assay, materials are incubated with human blood erythrocytes. As depicted in Fig. 13 materials exhibit hemolysis percentages below 20% at short incubation times, with SDS wells serving as reference for 100% hemolysis. Considering that optimal performance in biological environments typically entails less than 30% hemolysis,[49] it can be inferred that materials at short incubation times do not present significant drawbacks compared to blood erythrocytes.

However, at longer incubation periods, notably 24 hours, the percentage of hemolysis escalates, particularly evident in MSN-AP(10)-PPh_3^+-Sn material. Consequently, this material is excluded from future bacterial tests due to the considerable increase in hemolysis.

3.2.10. MTT assay. To assess the toxicity of the compounds before evaluating their potential *in vivo* activity in future studies, an MTT assay was conducted using the tin prodrug $SnPh_3Cl$ (the prodrug species included the final nanomaterials) on a healthy human embryonic kidney cell line (HEK 293T). As shown in Fig. S9 (ESI†), cell viability dropped to below 10% at a

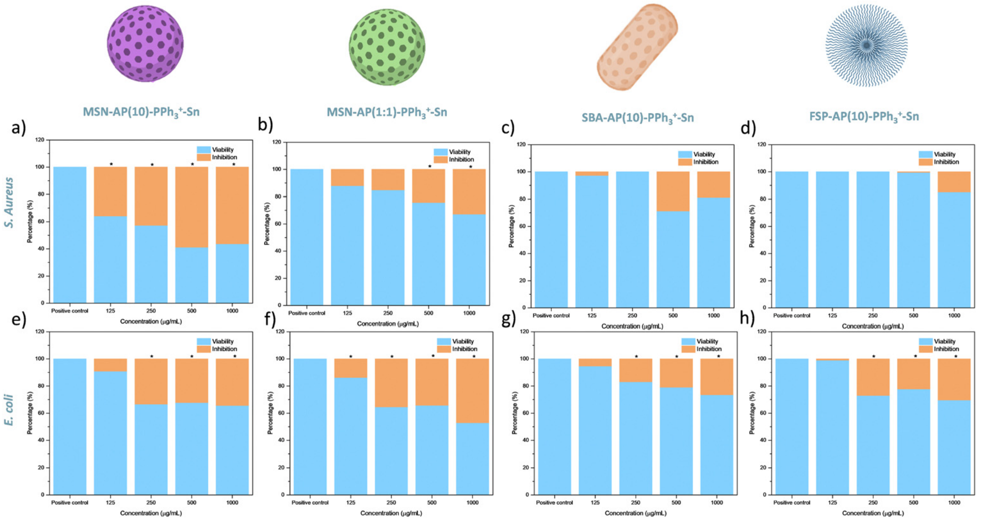

Fig. 11 Percentage inhibition of biofilms after incubation for 24 hours with the materials: *S. aureus* (a) MSN-AP(10)-PPh_3^+-Sn; (b) MSN-AP(1:1)-PPh_3^+-Sn; (c) SBA-AP(10)-PPh_3^+-Sn; (d) FSP-AP(10)-PPh_3^+-Sn and *E. coli* (e) MSN-AP(10)-PPh_3^+-Sn; (f) MSN-AP(1:1)-PPh_3^+-Sn; (g) SBA-AP(10)-PPh_3^+-Sn; (h) FSP-AP(10)-PPh_3^+-Sn ($* = p < 0.05$).

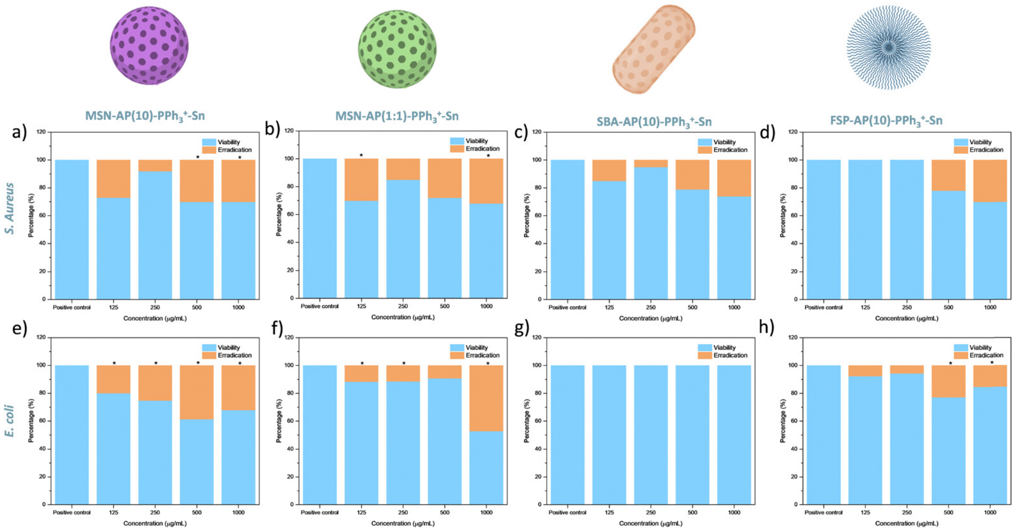

Fig. 12 Percentage eradication of biofilms after incubation for 24 hours with the materials: *S. aureus* (a) MSN-AP(10)-PPh_3^+-Sn; (b) MSN-AP(1:1)-PPh_3^+-Sn; (c) SBA-AP(10)-PPh_3^+-Sn; (d) FSP-AP(10)-PPh_3^+-Sn and *E. coli* (e) MSN-AP(10)-PPh_3^+-Sn; (f) MSN-AP(1:1)-PPh_3^+-Sn; (g) SBA-AP(10)-PPh_3^+-Sn; (h) FSP-AP(10)-PPh_3^+-Sn (* = $p < 0.05$).

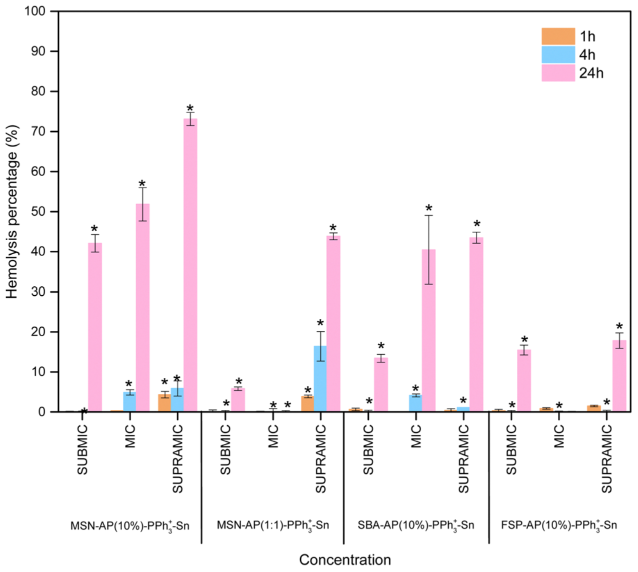

Fig. 13 Percentages of hemolysis obtained in the assay after incubation of erythrocytes with the final materials at SUBMIC, MIC and SUPRAMIC concentrations (* = $p < 0.05$).

concentration of only 1 μg mL^{-1} of the Sn compound, and approached 0% at higher concentrations. These results indicate that the Sn compound exhibits high toxicity and is unlikely to be used without incorporation into nanoparticles or other ligands to mitigate its toxic effects.

3.2.11. Resazurin assay. To assess the potential applicability of the nanostructured materials in future *in vivo* tests, it is essential to study their effects on human blood erythrocytes and their potential toxicity in the primary excretory organs, namely the liver and kidneys, which depend on the size of the nanoparticles. Consequently, a resazurin-based toxicity test was conducted on human embryonic kidney cells (HEK 293T).

The final materials, SBA-AP(10)-PPh_3^+-Sn and FSP-AP(10)-PPh_3^+-Sn, exhibited IC_{50} values of 48.33 μg mL^{-1} and 99.95 μg mL^{-1}, respectively, in terms of the final material, and 0.81 μg mL^{-1} and 1.90 μg mL^{-1}, respectively, in terms of tin concentration (see Fig. S10 of ESI†). When compared to the MTT assay results for the $SnPh_3Cl$ prodrug, it is evident that incorporating the tin compound within the nanoparticles significantly reduces its toxicity to healthy cells, increasing cell viability by more than 12 times. Thus, using silica nanostructured materials appears to be advantageous for applying the highly cytotoxic $SnPh_3$ moieties in biological environments (*in vitro*) and is expected to have a lesser impact on organs such as the kidneys. In this context and considering previous studies by our team, which demonstrated that analogous tin-functionalized silica-based nanomaterials are non-toxic to healthy cells *in vitro* and that kidney biomarkers in mice remain intact after nanoparticle treatment *in vivo*,[28,37,50] it can be concluded that the materials reported here, with their dual antitumoral and antibacterial (and antibiofilm) activity, warrant additional studies to confirm their potential although additional studies should be undertaken to be applied *in vivo*.

Conclusions

The synthesis and functionalization of final materials, namely MSN-AP(1:1)-PPh_3^+-Sn, SBA-AP(10)-PPh_3^+-Sn, and FSP-AP(10)-PPh_3^+-Sn, were successfully achieved, showcasing potent antibacterial activity against *S. aureus* and *E. coli* strains. Notably, the latter exhibited more promising outcomes, potentially attributed to the PPh_3^+ fragment's influence. Moreover, it was evident that the organotin(IV) complex serves as an effective treatment, as preceding materials lacked activity.

Oxidative stress emerged as a plausible mechanism of action for these materials even in the presence of GSH. Their low hemolysis percentages indicate promising prospects for future *in vivo* applications. Furthermore, observations from biofilm inhibition and eradication tests underscored a concentration-dependent relationship between material activity and efficacy. Particularly noteworthy is the outstanding biofilm inhibition exhibited by MSN-AP(10)-PPh_3^+-Sn against the *S. aureus* strain, hinting at its remarkable potential in combating bacterial biofilms.

In conclusion, these findings highlight the multifaceted antibacterial properties of the synthesized materials, suggesting their viability for diverse biomedical applications. Further exploration and refinement of these materials hold promise for combating bacterial infections and advancing therapeutic interventions.

In view of the outstanding properties of the studied organotin(IV)-based nanomaterial which are the first materials of this type showing a good degree of eradication in both *E.coli* and *S. aureus* biofilms, in our ongoing research, we are focusing our efforts in gaining additional insights on the antibacterial effect of this kind of systems to be applied in preclinical trials. Our current studies focus towards incorporating therapeutic agents aimed at enhancing wound healing. We are investigating whether our materials hold promise in the treatment of chronic wounds, which can arise from diverse underlying health conditions and are highly susceptible to infection due to compromised tissue integrity and impaired immune response. These conditions may stem from diseases such as diabetes mellitus, autoimmune disorders, or peripheral neuropathies. The future study of our innovative materials is focused, therefore, on offering a potential solution to address challenges associated with antibiotic resistance or limited efficacy of conventional antibiotics in the treatment of chronic wounds. In addition, although the toxicity studies show promising properties by the reduction of the toxicity of the tin prodrug after incorporation within the nanostructured materials, additional studies in this context should be undertaken to confirm the potential ability of the materials to be applied *in vivo*.

Data availability

The data supporting this article have been included as part of the ESI† or directly in the manuscript.

Conflicts of interest

There are no conflicts to declare.

Acknowledgements

We would like to thank funding from the research project PID2022-136417NB-I00 financed by Ministerio de Ciencia, Innovación y Universidades of Spain MCIU/AEI/10.13039/501100011033/ and ''ERDF A way of making Europe'', and from the Research Thematic Network RED2022-134091-T financed by Ministerio de Ciencia, Innovación y Universidades of Spain MCIU/AEI/10.13039/501100011033. We would also like to thank Universidad Rey Juan Carlos for the financial support of our research team COMET-NANO with the project M3271.

References

1 J. W. Bennett and K.-T. Chung, *Advances in Applied Microbiology*, Academic Press, 2001, **49**, 163–184.
2 K. Kaur, P. Barathe, S. Reddy, V. Mathur and V. Kumar, *Med. Plants Antimicrob. Ther.*, 2024, 1–21.
3 D. W. Kim and C. J. Cha, *Exp. Mol. Med.*, 2021, **53**, 301–309.
4 S. A. McEwen and P. J. Collignon, *Microbiol. Spectr.*, 2018, **6**, DOI: 10.1128/microbiolspec.arba-0009-2017.
5 B. Aslam, M. Khurshid, M. I. Arshad, S. Muzammil, M. Rasool, N. Yasmeen, T. Shah, T. H. Chaudhry, M. H. Rasool, A. Shahid, X. Xueshan and Z. Baloch, *Front. Cell. Infect. Microbiol.*, 2021, **11**, 771510.
6 S. Hernando-Amado, T. M. Coque, F. Baquero and J. L. Martínez, *Nat. Microbiol.*, 2019, **4**, 1432–1442.
7 N. B. Fernandes, Y. Nayak, S. Garg and U. Y. Nayak, *Coord. Chem. Rev.*, 2023, **478**, 214977.
8 Y. Wang, Q. Zhao, N. Han, L. Bai, J. Li, J. Liu, E. Che, L. Hu, Q. Zhang, T. Jiang and S. Wang, *Nanomedicine*, 2015, **11**, 313–327.
9 Y. Wang, K. Gou, X. Guo, J. Ke, S. Li and H. Li, *Acta Biomater.*, 2021, **123**, 72–92.
10 G. Yin, X. Chen, Q. Xu, X. Yang, P. Zhang and H. Wang, *Mater. Today Commun.*, 2024, **38**, 108555.
11 D. M. Dereje, A. García, C. Pontremoli, B. González, M. Colilla, M. Vallet-Regí, I. Izquierdo-Barba and N. Barbero, *Microporous Mesoporous Mater.*, 2024, **372**, 113096.
12 A. Bachvarova-Nedelcheva, Y. Kostova, L. Yordanova, E. Nenova, P. Shestakova, I. Ivanova and E. Pavlova, *Molecules*, 2024, **29**, 2675.
13 S. Wang, L. Fang, H. Zhou, M. Wang, H. Zheng, Y. Wang, M. D. Weir, R. Masri, T. W. Oates, L. Cheng, H. H. K. Xu and F. Liu, *Dent. Mater.*, 2024, **40**, 179–189.
14 I. Otri, S. Medaglia, R. Martínez-Máñez, E. Aznar and F. Sancenón, *Nanomaterials*, 2024, **14**, 228.
15 Y. Zhao, B. G. Trewyn, I. I. Slowing and V. S. Y. Lin, *J. Am. Chem. Soc.*, 2009, **131**, 8398–8400.
16 D. Zhao, Q. Huo, J. Feng, B. F. Chmelka and G. D. Stucky, *J. Am. Chem. Soc.*, 1998, **120**, 6024–6036.
17 S. M. Sadeghzadeh, R. Zhiani and S. Emrani, *RSC Adv.*, 2017, **7**, 24885–24894.
18 M. J. Mitchell, M. M. Billingsley, R. M. Haley, M. E. Wechsler, N. A. Peppas and R. Langer, *Nat. Rev. Drug Discovery*, 2021, **20**, 101–124.
19 D. Díaz-García, S. Prashar and S. Gómez-Ruiz, *Int. J. Mol. Sci.*, 2023, **24**, 2332.
20 S. Kim, N. G. Yoon, B. Jana, B. H. Kang and J. H. Ryu, *Bull. Korean Chem. Soc.*, 2022, **43**, 391–395.
21 M. Millard, D. Pathania, Y. Shabaik, L. Taheri, J. Deng and N. Neamati, *PLoS One*, 2010, **5**, e13131.

22 A. J. Martín-Rodríguez, J. M. F. Babarro, F. Lahoz, M. Sansón, V. S. Martín, M. Norte and J. J. Fernández, *PLoS One*, 2015, **10**, 123652.

23 S. Kang, K. Sunwoo, Y. Jung, J. K. Hur, K.-H. Park, J. S. Kim and D. Kim, *Antibiotics*, 2020, **9**, 758.

24 M. K. Ibrahim, A. Haria, N. V. Mehta and M. S. Degani, *Future Med. Chem.*, 2023, **15**, 2113–2141.

25 D. Díaz-García, K. Montalbán-Hernández, I. Mena-Palomo, P. Achimas-Cadariu, A. Rodríguez-Diéguez, E. López-Collazo, S. Prashar, K. Ovejero Paredes, M. Filice, E. Fischer-Fodor and S. Gómez-Ruiz, *Pharmaceutics*, 2020, **12**, 512.

26 M. Ugalde-Arbizu, J. J. Aguilera-Correa, V. García-Almodóvar, K. Ovejero-Paredes, D. Díaz-García, J. Esteban, P. L. Páez, S. Prashar, E. San Sebastian, M. Filice and S. Gómez-Ruiz, *Pharmaceutics*, 2023, **15**, 560.

27 A. Pompilio, M. Scocchi, M. L. Mangoni, S. Shirooie, A. Serio, Y. Ferreira Garcia da Costa, M. S. Alves, G. Şeker Karatoprak, I. Süntar, H. Khan and G. Di Bonaventura, *Crit. Rev. Microbiol.*, 2023, **49**, 117–149.

28 K. Ovejero Paredes, D. Díaz-García, V. García-Almodóvar, L. Lozano Chamizo, M. Marciello, M. Díaz-Sánchez, S. Prashar, S. Gómez-Ruiz and M. Filice, *Cancers*, 2020, **12**, 187.

29 CLSI (Clinical and Laboratory Standards Institute), 2018.

30 L. Wang, X. Han, J. Li, L. Qin and D. Zheng, *Powder Technol.*, 2012, **231**, 63–69.

31 D. Díaz-García, E. Fischer-Fodor, C. I. Vlad, J. M. Méndez-Arriaga, S. Prashar and S. Gómez-Ruiz, *Microporous Mesoporous Mater.*, 2021, **323**, 111238.

32 B. L. Tee and G. Kaletunç, *Biotechnol. Prog.*, 2009, **25**, 436–445.

33 T. C. Brown, A. Bagheri and C. M. Fellows, *Langmuir*, 2023, **39**, 1914–1926.

34 Z. Zhang and Z. Yang, *Chin. J. Catal.*, 2013, **34**, 1797–1810.

35 M. Thommes, K. Kaneko, A. V. Neimark, J. P. Olivier, F. Rodriguez-Reinoso, J. Rouquerol and K. S. W. Sing, *Pure Appl. Chem.*, 2015, **87**, 1051–1069.

36 D. Díaz-García, P. R. Ardiles, S. Prashar, A. Rodríguez-Diéguez, P. L. Páez and S. Gómez-Ruiz, *Pharmaceutics*, 2019, **11**, 30.

37 K. Ovejero-Paredes, D. Díaz-García, I. Mena-Palomo, M. Marciello, L. Lozano-Chamizo, Y. L. Morato, S. Prashar, S. Gómez-Ruiz and M. Filice, *Biomater. Adv.*, 2022, **137**, 212823.

38 M. O. Guerrero-Pérez and G. S. Patience, *Canadian J. Chem. Eng.*, 2020, **98**, 25–33.

39 F. S. Rocha, A. J. Gomes, C. N. Lunardi, S. Kaliaguine and G. S. Patience, *Canadian J. Chem. Eng.*, 2018, **96**, 2512–2517.

40 Y. Ishii, Y. Nishiwaki, A. Al-zubaidi and S. Kawasaki, *J. Phys. Chem. C*, 2013, **117**, 18120–18130.

41 J. Karges, D. Díaz-García, S. Prashar, S. Gómez-Ruiz and G. Gasser, *ACS Appl. Bio Mater.*, 2021, **4**, 4394–4405.

42 A. Toranzo, P. S. Bustos, M. G. Ortega, P. L. Páez and C. Lucero-Estrada, *J. Appl. Microbiol.*, 2022, **132**, 209–220.

43 T. Chautrand, D. Souak, S. Chevalier and C. Duclairoir-Poc, *Microorganisms*, 2022, **10**, 924.

44 S. K. Priyadarshini, M. Murugesan, R. D. Michael, P. Aiya Subramani and P. Rajendran, *Fish Shellfish Immunol.*, 2023, **142**, 109141.

45 Y. F. Huang, Y. Li, J. Y. Chen, J.-H. Lin, L. Liu, J.-Z. Ye and Y.-B. Su, *Biochem. Biophys. Res. Commun.*, 2022, **625**, 134–139.

46 M. A. Quinteros, C. A. Viviana, R. Onnainty, V. S. Mary, M. G. Theumer, G. E. Granero, M. G. Paraje and P. L. Páez, *Int. J. Biochem. Cell Biol.*, 2018, **104**, 87–93.

47 M. Ugalde-Arbizu, J. J. Aguilera-Correa, A. Mediero, J. Esteban, P. L. Páez, E. San Sebastian and S. Gómez-Ruiz, *Pharmaceuticals*, 2022, **15**, 884.

48 I. Park, A. Jailani, J. H. Lee, B. Ahmed and J. Lee, *Pharmaceutics*, 2023, **15**, 1679.

49 A. G. Veiko, E. Olchowik-Grabarek, S. Sekowski, A. Roszkowska, E. A. Lapshina, I. Dobrzynska, M. Zamaraeva and I. B. Zavodnik, *Molecules*, 2023, **28**, 1252.

50 P. C. Choudante, J. Mamilla, L. Kongari, D. Díaz-García, S. Prashar, S. Gómez-Ruiz and S. Misra, *J. Drug Delivery Sci. Technol.*, 2024, **94**, 105502.